AGU PUBLICATIONS

Global Biogeochemical Cycles

RESEARCH ARTICLE
10.1002/2015GB005189

Key Points:
- Notable seasonal cycle in surface ocean δ^{30}Si to be considered in interpretation of measurements
- Sediment δ^{30}Si reflects exported signal from euphotic zone
- Role of sedimentary δ^{30}Si in bottom ocean through dissolution and diffusion

Supporting Information:
- Figure S1
- Figure S2
- Figure S3
- Figure S4
- Texts S1 and S2 and Captions of Figures S1–S4

Correspondence to:
S. Gao,
Shuang.Gao@gfi.uib.no

Citation:
Gao, S., D. A. Wolf-Gladrow, and C. Völker (2016), Simulating the modern δ^{30}Si distribution in the oceans and in marine sediments, *Global Biogeochem. Cycles*, *30*, 120–133, doi:10.1002/2015GB005189.

Received 11 MAY 2015
Accepted 12 JAN 2016
Accepted article online 14 JAN 2016
Published online 1 FEB 2016

Simulating the modern δ^{30}Si distribution in the oceans and in marine sediments

S. Gao[1,2], D. A. Wolf-Gladrow[1], and C. Völker[1]

[1]Department of Biogeosciences, Alfred-Wegener-Institut Helmholtz-Zentrum für Polar- und Meeresforschung, Bremerhaven, Germany, [2]Now at Geophysical Institute, University of Bergen, Bergen, Norway

Abstract The δ^{30}Si of biogenic silica ($\delta^{30}Si_{BSi}$) in marine sediments is a promising proxy for the reconstruction of silicic acid utilization by diatoms in the geological past. The application of this proxy, however, requires an understanding of the modern δ^{30}Si distributions and their controlling mechanisms. Here we present results from a modern climate simulation with a coupled ocean-sediment model that includes a prognostic formulation of biogenic silica production with concurrent silicon isotopic fractionation. In agreement with previous studies, biological fractionation combined with physical transport and mixing determines the oceanic distribution of simulated δ^{30}Si. A new finding is a distinct seasonal cycle of δ^{30}Si in the surface ocean, which is inversely related to that of silicic acid concentration and mixed layer depth. We also provide the first simulation results of sedimentary δ^{30}Si, which reveal that (1) the $\delta^{30}Si_{BSi}$ distribution in the surface sediment reflects the exported $\delta^{30}Si_{BSi}$ signal from the euphotic zone and (2) the dissolution of biogenic silica in the sediment acts as a source of relatively light δ^{30}Si into the bottom waters of the polar oceans, while it is a source of heavier δ^{30}Si to the subtropical South Atlantic and South Pacific.

1. Introduction

The silicon isotopic composition δ^{30}Si can be defined as $\left[\frac{(^{30}Si/^{28}Si)_{sample}}{(^{30}Si/^{28}Si)_{NBS-28}} - 1\right] \cdot 10^3$ in per mil units. The δ^{30}Si of diatom frustules has been applied extensively for investigating glacial silicic acid utilization in the Southern Ocean, often in the context of explaining the low pCO_2 levels during the glacial period [*De La Rocha et al.*, 1998; *Brzezinski et al.*, 2002; *Beucher et al.*, 2007; *Pichevin et al.*, 2009; *Ellwood et al.*, 2010]. Diatoms contribute up to half of the modern oceanic primary production [*Nelson et al.*, 1995] and much of the export of organic carbon from the surface waters [*Dugdale et al.*, 1995; *Buesseler*, 1998; *Smetacek*, 1999]. During the formation of diatom frustules, the lighter Si isotopes are taken up and incorporated preferentially into frustules, leaving the remaining silicic acid in water enriched in the heavier stable isotopes of Si. Given a finite pool of silicic acid, the continued preferential uptake of, e.g., ^{28}Si by diatoms will result in a progressive increase in the relative abundance of the heavier isotopes in both dissolved and biogenic silica. In other words, the isotopic composition of silicic acid and of the opaline frustules increases as silicic acid utilization increases. Variations in the δ^{30}Si of the opaline frustules that are buried in the sediments may therefore reflect the extent of silicic acid depletion in the surface water at the time when the frustules were formed. Thus, δ^{30}Si holds a great potential as a proxy for investigation of marine silicic acid utilization by diatoms in the geological past. Application of this proxy requires a thorough understanding of the processes governing the modern marine δ^{30}Si distribution. However, the interplay of the local biological fractionation process with oceanic circulation and mixing makes interpretation of field observations with small sample sizes a challenge.

The instantaneous fractionation, ϵ, between silicic acid and biogenic silica during the formation of diatom frustules has been evaluated by various laboratory studies. *De La Rocha et al.* [1997] found a value of -1.1 ± 0.4‰ independent of temperature (12–22°C), growth rate, or diatom species for the three different species tested. In addition, *Milligan et al.* [2004] could show that ϵ is independent of the ambient pCO_2 level (100–750 µatm), which supports a broader use of the proxy δ^{30}Si under various environmental conditions. However, a recent laboratory study has revealed some species dependency of ϵ (ranging from −0.54 to −2.09‰) during diatom opal formation, which draws attention to diatom taxonomic analysis when using δ^{30}Si for reconstruction of Si utilization [*Sutton et al.*, 2013].

Many field studies have investigated the in situ variability of ϵ for diatom opal formation [*De La Rocha et al.*, 2000; *Varela et al.*, 2004; *Cardinal et al.*, 2005; *Reynolds et al.*, 2006; *De La Rocha et al.*, 2011; *Cavagna et al.*, 2011]

or dissolution [*Demarest et al.*, 2009; *Beucher et al.*, 2011] with respect to using either the "Rayleigh model" (a water mass isolated over the time span of a diatom bloom, also known as "closed system model") or the "open system model" (an open water mass with continuous input of silicic acid throughout the diatom bloom). Progress has also been made by field studies on mechanisms that control δ^{30}Si distribution and variation, such as physical mixing, opal dissolution, or iron availability, and further on the implication of δ^{30}Si distribution for tracing oceanic Si cycling [*Cardinal et al.*, 2005, 2007; *Reynolds et al.*, 2006; *Beucher et al.*, 2011; *Fripiat et al.*, 2011a, 2011b, 2012; *de Souza et al.*, 2012a, 2012b].

Modeling studies, on the other hand, provide overview and systematic approaches for understanding δ^{30}Si distribution and controlling mechanisms, because they calculate isotopic fractionation without explicit assumption of Rayleigh or open system model. *Wischmeyer et al.* [2003] calculated an overall oceanic distribution of silicon isotopes using a three-dimensional global ocean circulation and biogeochemistry model for the first time. Their work revealed that the relationship between silicic acid concentration and its δ^{30}Si is not a simple Rayleigh distillation curve. They also investigated the applicability of the correlation between silicic acid concentration in the surface water and the $\delta^{30}Si_{BSi}$ in the sediment for estimating the absolute silicic acid concentrations in the past. However, their model results did not show significant δ^{30}Si variations between the deep Atlantic and deep Pacific, which disagreed with observations [*De La Rocha et al.*, 2000]. Using a seven-box model, *Reynolds* [2009] simulated a 0.3‰ difference between the δ^{30}Si of the deep water masses of North Atlantic and North Pacific. A recent modeling study with a general circulation model (GCM) including Fe-dependent Si:N uptake ratio showed also a deep δ^{30}Si gradient between the North Atlantic and the Southern Ocean [*Matsumoto et al.*, 2013]. *De Souza et al.* [2014] investigated the physical and biogeochemical controls on the δ^{30}Si distribution in the deep oceanic interior, by parsing dissolved Si into its preformed and regenerated components in their model. Their study helps explain the observed δ^{30}Si difference between ocean basins and the strong physical control on the oceanic δ^{30}Si distribution. *Holzer and Brzezinski* [2015] further quantified the contributions of preformed and regenerated silicic acid to δ^{30}Si distribution and traced the origin regions of the preformed and regenerated δ^{30}Si.

In this study we first show that our model is able to reproduce the observed global patterns in δ^{30}Si and it agrees with the previous studies [*Cardinal et al.*, 2005; *Reynolds et al.*, 2006; *Beucher et al.*, 2008, 2011; *Reynolds*, 2009; *de Souza et al.*, 2014; *Brzezinski and Jones*, 2015; *Holzer and Brzezinski*, 2015] on the controlling mechanisms. We then focus on two major questions that remain unanswered by the previous global modeling studies of δ^{30}Si, namely, on the roles of seasonality and of the sediment.

In this manuscript, DSi and BSi refer to silicic acid and biogenic opal/biogenic silica, respectively.

2. Model Description

To simulate the biogeochemical cycle and the isotopic composition of silicon, we applied the Hamburg ocean carbon cycle model, version 5.1 (HAMOCC5.1) [*Six and Maier-Reimer*, 1996], which includes an interactive sediment module [*Heinze et al.*, 1999], coupled with an ocean general circulation model (OGCM) and the Max Planck Institute Global Ocean/Sea-Ice Model (MPI-OM) [*Marsland et al.*, 2003].

2.1. The Ocean Circulation Model

The ocean general circulation model used for this work, the Max Planck Institute Global Ocean/Sea-Ice Model (MPI-OM) [*Marsland et al.*, 2003], is based on the primitive equations that represent dynamical and thermodynamic processes. The model is forced by daily mean fields of heat, freshwater, and momentum fluxes, provided by the German Ocean Model Intercomparison Project (http://www.omip.zmaw.de). In order to get the highest resolution near the main deep water formation regions, which are essential for thermohaline circulation and climate change, one pole of the curvilinear coordinate system is placed over Greenland and the other over Antarctica. The spatial discretization with an orthogonal curvilinear C grid results in an average horizontal resolution of 6°. The model has 20 vertical levels (four levels in the upper 90 m) with level thickness increasing with depth. The time step is 3 h. The model includes subgrid-scale parameterizations for bottom boundary layer slope transport [*Legutke and Maier-Reimer*, 2002], horizontal and vertical viscosities, vertical and isopycnal diffusivities, eddy-induced mixing [*Gent et al.*, 1995], and convection. All biogeochemical tracers are fully advected and mixed by the OGCM. A detailed description of MPI-OM can be found online (http://www.mpimet.mpg.de/en/science/models/mpiom.html).

Table 1. Parameters Used in the Biological Model HAMOCC5.1

Model Parameter	Value
Constant O_2:P stoichiometric ratio: $R_{O_2:P}$	172 mol O_2 mol^{-1} P
Constant C:P stoichiometric ratio: $R_{C:P}$	122 mol C mol^{-1} P
Constant N:P stoichiometric ratio: $R_{N:P}$	16 mol N mol^{-1} P
Constant Fe:P stoichiometric ratio: $R_{Fe:P}$	3.66×10^{-4} mol Fe mol^{-1} P
Constant Si:P stoichiometric ratio: $R_{Si:P}$	25 mol Si mol^{-1} P
Global riverine input of Si	9.0 Tmol Si yr^{-1}
Global riverine input of $CaCO_3$	10.8 Tmol C yr^{-1}
Global riverine input of POC	1.1 Tmol P yr^{-1}
Half saturation constant for $Si(OH)_4$ uptake: $K_{PHY}^{Si(OH)_4}$	4.0 µmol L^{-1}
Converting rate constant from available silicic acid to opal production: r_{Pro}	0.5 per day
Constant sinking speed of detritus: w_{DET}	5 m d^{-1}
Constant sinking speed of opal: w_{opal}	10 m d^{-1}
Constant sinking speed of $CaCO_3$: w_{CaCO_3}	30 m d^{-1}
Opal redissolution rate constant, water column	3.0×10^{-3} per day
$CaCO_3$ redissolution rate constant, water column	0.075 per day
POC remineralization rate constant, water column	0.025 per day
DOC remineralization rate constant, water column	0.004 per day
$Si(OH)_4$ saturation concentration	1000 µmol L^{-1}
Opal redissolution rate constant, sediment	1.0×10^{-3} (kmol Si $m^{-3})^{-1}$ s^{-1}
$CaCO_3$ redissolution rate constant, sediment	1.0×10^{-7} (kmol C $m^{-3})^{-1}$ s^{-1}
POC remineralization rate constant, sediment	1.16×10^{-7} (kmol O $m^{-3})^{-1}$ s^{-1}
Diffusion coefficient, pore waters	1.0×10^{-9} m^2 s^{-1}
Characteristic temperature for opal dissolution: T_c	12°C
Species-dependent factor for opal dissolution: A	3.0×10^{-3} per day

2.2. The Biogeochemical Model

The biogeochemical model HAMOCC5.1 is derived originally from the work of *Six and Maier-Reimer* [1996]. HAMOCC5.1 is a complex Nutrient Phytoplankton Zooplankton Detritus model, with 5 biogeochemical tracers in the atmosphere, 25 in the water column, and 19 in the sediment in the standard model setup. The interactions between the cycling of C, N, P, Fe, and O_2 are simulated assuming constant stoichiometric ratios for C:N:P:O_2 [*Redfield et al.*, 1963]. The Si cycle is described further below. The most important model parameters are listed in Table 1. For a complete technical description of HAMOCC5.1, readers are referred to the model documentation by *Maier-Reimer et al.* [2005].

In the euphotic zone, phytoplankton growth depends on the availability of light and on the most limiting nutrient among phosphate, nitrate, and iron, as described by a Monod-type equation

$$P_{phy} = \frac{PHY \cdot J(I) \cdot X}{K_{PHY}^{PO_4} + X} \text{ with} \tag{1}$$

$$X = \min\left(PO_4, \frac{NO_3}{R_{N:P}}, \frac{Fe}{R_{Fe:P}}\right). \tag{2}$$

Here P_{phy} denotes phytoplankton growth rate by photosynthesis (expressed in kmol P m^{-3} d^{-1}), PHY is phytoplankton biomass concentration (kmol P m^{-3}), and J indicates a maximum phytoplankton growth rate (per day) under a certain availability of solar radiation I (W m^{-2}). PO_4 (kmol P m^{-3}) and NO_3 (kmol N m^{-3}) are concentrations of phosphate and nitrate, respectively. Fe is the dissolved iron concentration (kmol Fe m^{-3}), and $R_{N:P}$ (mol N (mol P)$^{-1}$) and $R_{Fe:P}$ (mol Fe (mol P)$^{-1}$) denote constant N:P and Fe:P stoichiometric ratios, respectively.

It is assumed that phytoplankton consists of diatoms, coccolithophorids, and others that produce neither calcareous or siliceous shells, although there is no explicit phytoplankton classification in the model. When silicate is available, diatom opal production is first computed proportionally to particulate organic matter production as

$$P_{Si} = \min\left(\frac{\Delta DET}{\Delta t} \cdot R_{Si:P} \cdot \frac{Si(OH)_4}{K_{PHY}^{Si(OH)_4} + Si(OH)_4}, r_{Pro} \cdot Si(OH)_4\right), \quad (3)$$

where P_{Si} denotes biogenic opal production rate (kmol Si m^{-3} d^{-1}), $\Delta DET/\Delta t$ denotes particulate organic matter production rate (kmol P m^{-3} d^{-1}), $R_{Si:P}$ is the biogenic opal to organic matter production ratio (mol Si (mol P)$^{-1}$), $K_{PHY}^{Si(OH)_4}$ indicates the half saturation constant for $Si(OH)_4$ uptake (kmol Si m^{-3}), and r_{Pro} is a rate constant (per day) for opal production under silicic acid nonlimiting conditions. The remaining fraction of the particulate organic matter production is accompanied by the production of calcareous shells by coccolithophorides.

Dissolution of opaline frustules proceeds according to a temperature-dependent function [*Kamatani*, 1982; *Gnanadesikan*, 1999] as

$$r = A \cdot \exp(T/T_c), \quad (4)$$

where r indicates the diatom opal dissolution rate (per day). In nature A is a species-dependent rate, but in the model it is a constant that has been tuned within the range given by *Kamatani* [1982] such that the model presents the most realistic vertical distribution of silicic acid. T (°C) denotes temperature and T_c (°C) stands for critical temperature. Both A and T_c are listed in Table 1. According to the values of A and T_c, the range of opal dissolution length scales would be around 955 to 2596 m depending on the ocean temperature.

2.3. The Sediment Model

In the model it is assumed that particles (organic detritus, opal, calcium carbonate, and dust) are not horizontally transported. They settle down through the water column with constant sinking speeds (see Table 1) and are remineralized and dissolved on the way downward. Those particles that have escaped degradation reach the ocean floor. Together with nutrient concentrations in the bottom ocean layer, these fluxes become the upper boundary condition for the sediment model. The sediment model [*Heinze et al.*, 1999] simulates particle accumulation, decomposition of detritus, redissolution of opal and calcium carbonate, and the vertical diffusion of pore water tracers. The simultaneous dissolution and diffusion processes are calculated by an implicit numerical scheme. The model contains 12 biologically active sediment layers with increasing layer thickness and decreasing porosity from top to bottom. To maintain a constant porosity profile, the particulate matter is shifted downward and stored in an additional diagenetically consolidated layer (the thirteenth layer), representing the materials leaving the ocean biogeochemical cycle for permanent burial. At model steady state, this mass loss of the whole ocean sediment system is balanced by riverine input.

2.4. Silicon Isotopic Fractionation

In order to investigate the $\delta^{30}Si$ distribution, we incorporated the cycling of the silicon isotope ^{30}Si into HAMOCC5.1 in addition to that of the total Si (the sum of the stable isotopes ^{28}Si, ^{29}Si, and ^{30}Si) which already existed in the model. The heavier isotope ^{30}Si is fractionated against during diatom frustules production and potentially also during frustules dissolution as follows:

$$P_{^{30}Si}^{t} = P_{Si}^{t} \cdot \alpha_1 \cdot \frac{[^{30}Si(OH)_4]^{t-1}}{[Si(OH)_4]^{t-1}}, \quad (5)$$

$$D_{^{30}Si}^{t} = D_{Si}^{t} \cdot \alpha_2 \cdot \frac{[B^{30}Si]^{t-1}}{[BSi]^{t-1}}, \quad (6)$$

where t and $t-1$ are consecutive time levels. P_{Si} and $P_{^{30}Si}$ are biogenic Si and ^{30}Si production rates (kmol Si m^{-3} d^{-1}), respectively, and $\alpha_1 = 0.9989$ [*De La Rocha et al.*, 1997] denotes the fractionation factor for biogenic Si production. D_{Si} and $D_{^{30}Si}$ are the dissolution rates (kmol Si m^{-3} d^{-1}) of biogenic Si and ^{30}Si, respectively, and α_2 is either equal to 1, assuming no fractionation during BSi dissolution, or equal to 0.99945 [*Demarest et al.*, 2009], assuming fractionation during BSi dissolution. In this work, we assume no fractionation during biogenic Si dissolution except one set of data in Figure 9. Detailed information on the model run including fractionation during biogenic Si dissolution is given by *Gao* [2014].

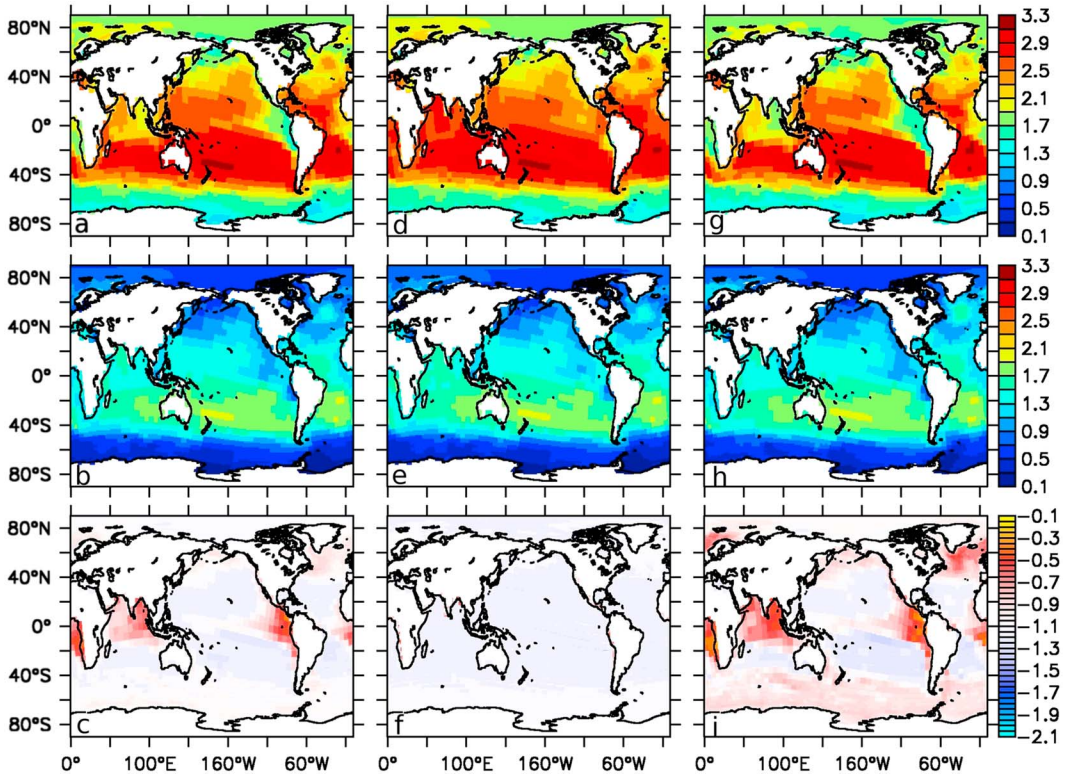

Figure 1. Simulated δ^{30}Si (‰) of (a, d, g) silicic acid, (b, e, h) biogenic opal, and the (c, f, i) difference between biogenic opal and silicic acid. (Figures 1a–1c) Within euphotic zone (upper 90 m in the model), (Figures 1d–1f) within euphotic zone and also above the annual mixed layer depth, and (Figures 1g–1i) within euphotic zone but below the annual mixed layer depth.

The $(^{30}Si/^{28}Si)_{NBS-28}$ reference value that has been used to calculate δ^{30}Si in this work is 0.0335 [*Coplen et al.*, 2002].

2.5. Model Initialization and Riverine Input

The oceanic silicic acid distribution is initialized with a profile obtained by averaging the World Ocean Atlas 2009 (WOA09) data set horizontally [*Garcia et al.*, 2010] (http://www.nodc.noaa.gov/cgi-bin/OC5/WOA09/woa09.pl). According to the in situ measurements given by *De La Rocha et al.* [2000], we initialized the $\delta^{30}Si_{DSi}$ and $\delta^{30}Si_{BSi}$ with homogeneous values of +1.1‰ and +1.0‰, respectively.

The riverine input of Si, in form of silicic acid, is evenly supplied in the model over the whole ocean surface every model time step with a uniform isotopic composition of +0.8‰ [*De La Rocha et al.*, 2000]. This approximation of distribution of riverine input of Si may smooth the horizontal gradient of $\delta^{30}Si_{DSi}$ in the surface water between the coastal regions with a supply of relatively low δ^{30}Si by rivers and the nutrient-depleted subtropical gyres with high δ^{30}Si. Although detailed distributions of riverine silicate input into a coastal zone have been published [*Bernard et al.*, 2011; *Dürr et al.*, 2011], a comprehensive data set of δ^{30}Si of the input is not available yet.

3. Results

The model is in a quasi steady state with repeating annual cycle after 10,000 model years. All calculations in this paper are made using the output of the single model year 10,000, since there is little intrinsic interannual variability. By then the globally averaged oceanic concentration of silicic acid is 82 μmol L^{-1}, which is in close agreement with the estimate of *Sarmiento and Gruber* [2006] of 84 μmol L^{-1} and falls between the estimate of *Tréguer and De La Rocha* [2013] of ~75 μmol L^{-1} and that of the WOA09 data set of 92 μmol L^{-1} [*Garcia et al.*, 2010]. The steady state global mean $\delta^{30}Si_{DSi}$ amounts to +1.3‰ in the model.

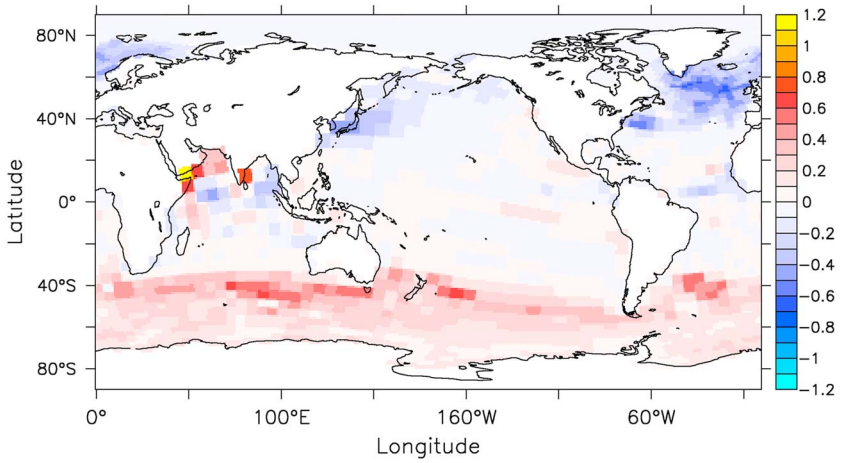

Figure 2. Difference in surface δ^{30}Si (‰) of silicic acid between March and September.

3.1. The Simulated δ^{30}Si Distribution

Annual average values of $\delta^{30}Si_{DSi}$ in the upper 90 m range from +1.20 to +3.15‰ with the higher values occurring in the subtropical gyres (Figure 1a), where silicic acid is depleted. The pattern of averaged δ^{30}Si of biogenic opal over the upper 90 m is very similar to that of $\delta^{30}Si_{DSi}$, but the absolute values range from +0.15 to +1.95‰ (Figure 1b).

The model shows a distinct seasonal pattern of surface $\delta^{30}Si_{DSi}$ especially in high latitudes. In the Northern Hemisphere north of ~40°N, surface $\delta^{30}Si_{DSi}$ reaches its lowest value in March and highest in September, while in the Southern Hemisphere (south of ~40°S) it is the opposite. The difference in $\delta^{30}Si_{DSi}$ between winter and summer can reach up to 0.7‰ both in the North Atlantic and in the Southern Ocean (Figure 2).

The $\delta^{30}Si_{DSi}$ distribution is relatively uniform in the deep Pacific Ocean, whereas it shows a considerable variability in the deep Atlantic Ocean, with the North Atlantic Deep Water (NADW) carrying a relatively high $\delta^{30}Si_{DSi}$ signal (~ +1.3‰) (Figure 3 and Figure S3 in the supporting information).

The δ^{30}Si of silicic acid in the ocean bottom layer ranges from +1.1 to +2.6‰, with the average values of +1.55‰ in the Arctic Ocean and +1.20‰ in the rest of the ocean basins (Figure 4a). The higher values occur in the Arctic Ocean as well as near continental margins. In the sediment surface layer, $\delta^{30}Si_{DSi}$ of pore water and $\delta^{30}Si_{BSi}$ range from +0.25 to +1.85‰ (Figure 4b) and from +0.20 to +1.95‰ (Figure 5a), respectively.

3.2. Model Validation: Model-Observation Comparison

In the last decade, the number of in situ measurements of δ^{30}Si has been growing rapidly, especially after the GEOTRACES Project (http://www.geotraces.org/) has been launched. The expansion of the silicon isotope

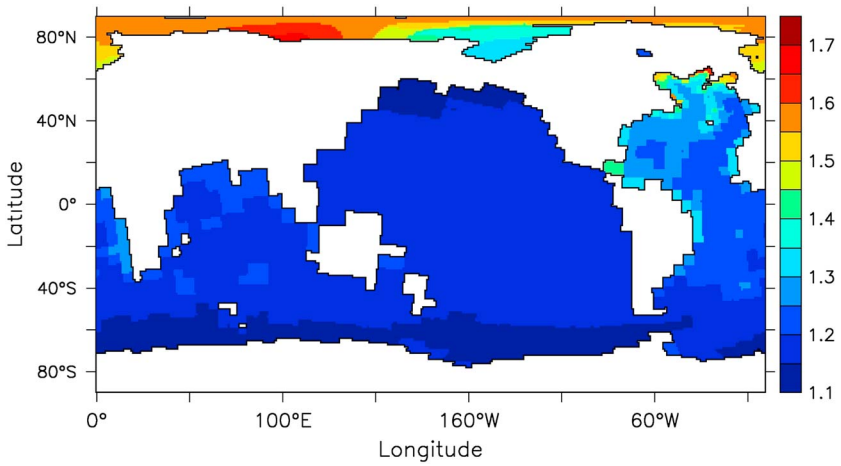

Figure 3. The δ^{30}Si (‰) of silicic acid at 2000 m water depth.

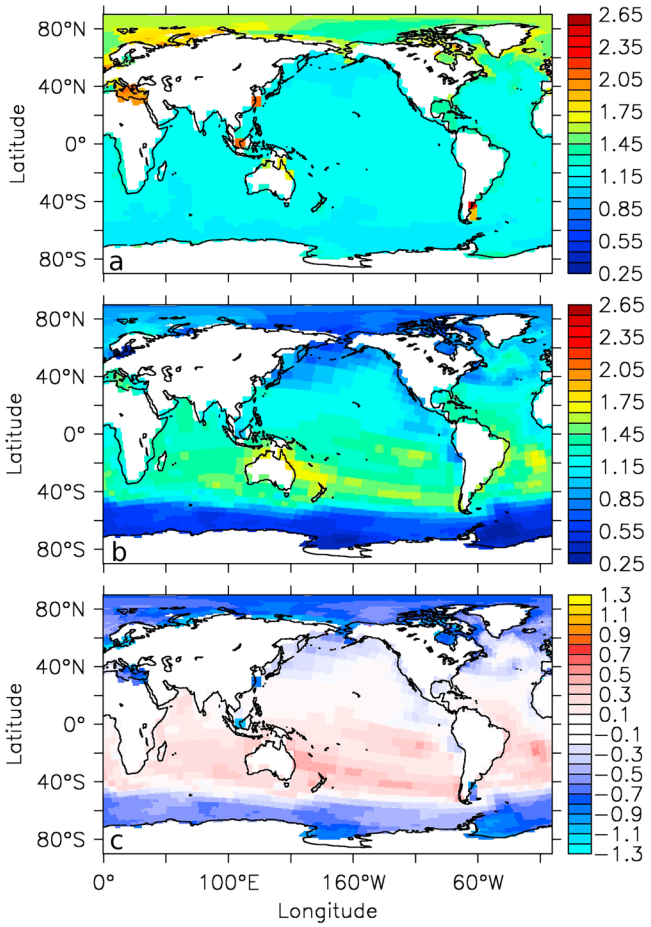

Figure 4. (a) The δ^{30}Si (‰) of silicic acid in the ocean bottom layer. (b) The δ^{30}Si (‰) of silicic acid in pore water in the sediment surface layer. (c) The difference between Figures 4b and 4a.

database provides the possibility of a comparison between observational data and model results. Here we compare the measured and modeled DSi concentrations and $\delta^{30}Si_{DSi}$ both in the surface water (averaged between 0 and 100 m) and in the deep water (averaged between 2000 m and the ocean bottom).

The simulated DSi concentration and $\delta^{30}Si_{DSi}$ in the surface ocean compare well to the in situ measurements with the exception of a few locations in the North Pacific and the Southern Ocean (Figures 6a and 6c). This discrepancy is probably attributed to the seasonal signal of the observational data contrasting to the annual

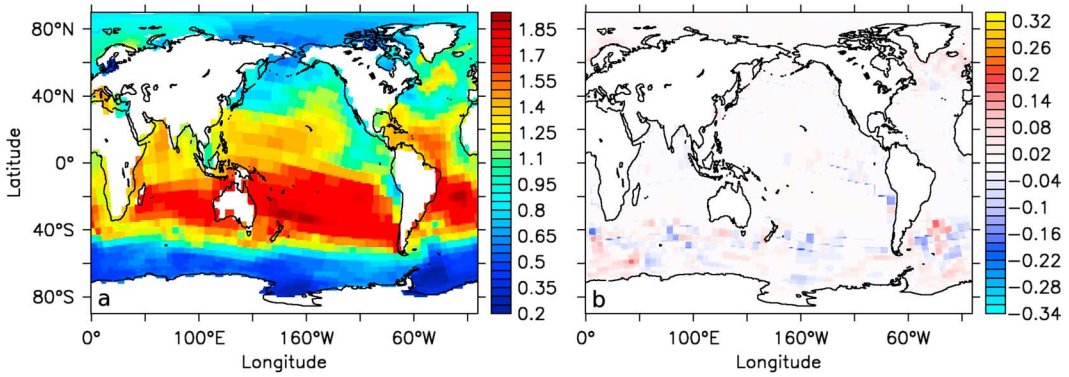

Figure 5. (a) The δ^{30}Si of biogenic opal (‰) in the sediment surface layer. (b) The difference between Figure 5a and the δ^{30}Si of opal fluxes sinking out of the euphotic zone (crossing 90 m).

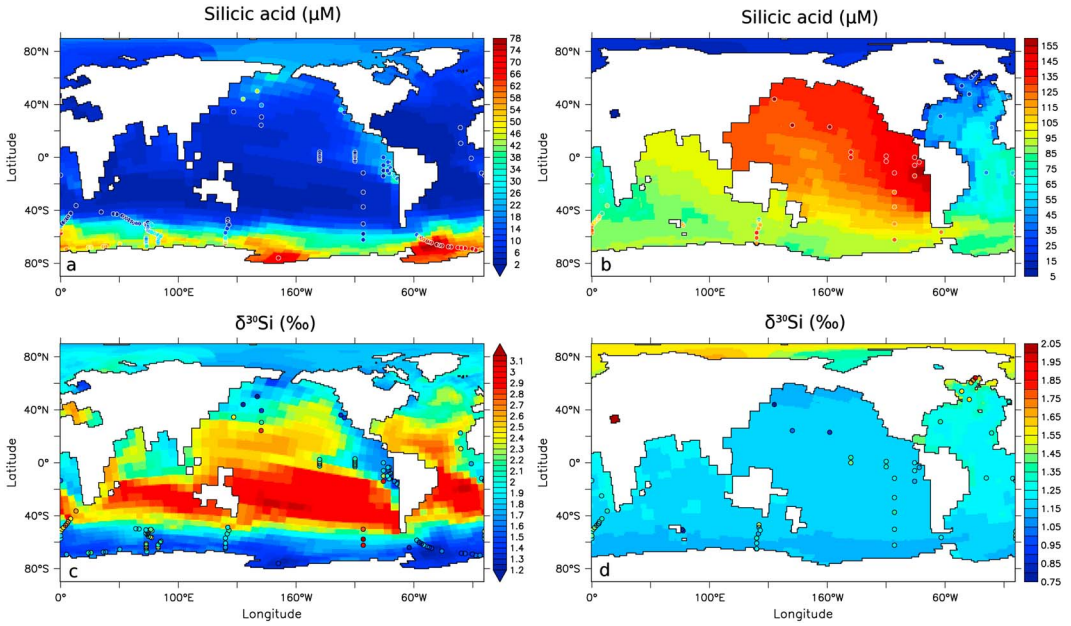

Figure 6. In situ measurements (colored dots) plotted over model results: (a) silicic acid concentration (μmol L^{-1}) averaged in upper 100 m water column, (b) silicic acid concentration (μmol L^{-1}) averaged between 2000 m and the sea floor, (c) δ^{30}Si of silicic acid (‰) averaged in upper 100 m water column, and (d) δ^{30}Si of silicic acid (‰) averaged between 2000 m and the sea floor. In situ data are taken from *Beucher et al.* [2008, 2011], *Cardinal et al.* [2005], *De La Rocha et al.* [2000, 2011], *de Souza et al.* [2012a, 2012b], *Ehlert et al.* [2012], *Fripiat et al.* [2011a, 2011b, 2012], *Grasse et al.* [2013], and *Reynolds et al.* [2006].

mean values of the model. In the deep ocean, the simulated DSi concentrations are higher than observed in the Atlantic and lower in the Pacific and the Southern Ocean (Figures 6b and 6d). This reflects some deficiencies of the coarse resolution ocean circulation model such as the too shallow Atlantic Deep Water and the too strong invasion of Antarctic Bottom Water into the north deep Atlantic (Figure S2).

The modeled $\delta^{30}Si_{DSi}$ values are significantly correlated with the observed values ($r = 0.69$), especially in the upper ocean (Figure 7). Close to the ocean bottom, modeled $\delta^{30}Si_{DSi}$ values are rather uniform compared to the observed ones.

4. Discussion

4.1. Control of δ^{30}Si Spatial Distributions in the Ocean

4.1.1. Si-$\delta^{30}Si_{DSi}$ in the Surface Ocean

In surface waters one often observes an inverse relationship between the concentration of silicic acid and its isotopic composition δ^{30}Si [*De La Rocha et al.*, 2011; *de Souza et al.*, 2012a; *Brzezinski and Jones*, 2015]. Plotting the modeled annual average of these two variables against each other shows a nonlinear relationship in different ocean basins (Pacific, Atlantic, Southern Ocean, and Indian Ocean) (Figure 8a). The $\delta^{30}Si_{DSi}$ increases with a decrease in silicic acid concentration, demonstrating the primary control of biological fractionation on the surface $\delta^{30}Si_{DSi}$ distribution. Figure 8b shows the natural logarithm of silicic acid concentration versus the corresponding $\delta^{30}Si_{DSi}$ in different ocean basins, and they all show approximately linear relations. In an ideal Rayleigh system, the slope of the linear relation would be equal to the biological fractionation ϵ. In the model, the slopes are generally smaller than ϵ and vary between ocean basins. This shows that physical transport through advection and diffusion invalidates the prerequisite of a closed system, which is required for Rayleigh fractionation to occur, throughout the oceans.

We thus agree with previous studies [*Cardinal et al.*, 2005; *Reynolds et al.*, 2006; *Beucher et al.*, 2008, 2011] that it is the combination of biological fractionation during BSi production and physical transport that determines $\delta^{30}Si_{DSi}$ in the surface waters.

4.1.2. $\delta^{30}Si_{DSi}$ and $\delta^{30}Si_{BSi}$ in the Surface Ocean

In the euphotic zone, the biological fractionation during production is the intrinsic controlling factor of $\delta^{30}Si_{DSi}$ and $\delta^{30}Si_{BSi}$. The spatial distributions of $\delta^{30}Si_{DSi}$ and $\delta^{30}Si_{BSi}$, however, are influenced by ocean physical param-

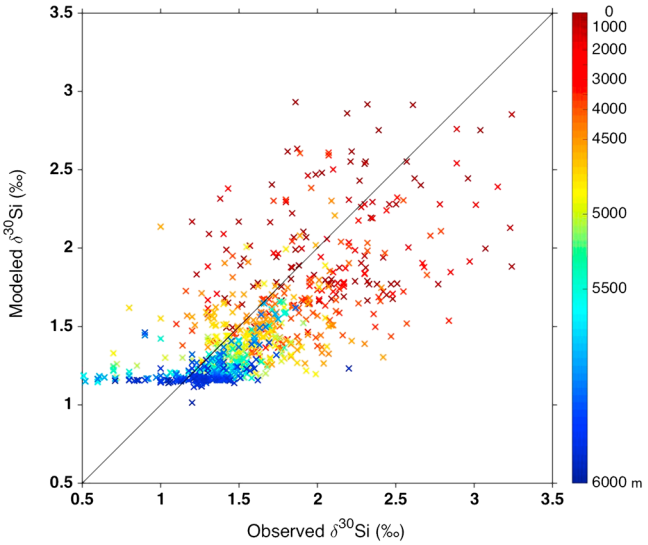

Figure 7. The modeled versus observed δ^{30}Si (‰) of silicic acid (correlation coefficient $r = 0.69$). The black line is the 1:1 line. Colors indicate water depths. An extremely high value of 4.36‰ in the observation has been removed from the plot and the calculation of correlation coefficient. Observational data are taken from *Beucher et al.* [2008, 2011], *Cardinal et al.* [2005], *De La Rocha et al.* [2000, 2011], *de Souza et al.* [2012a, 2012b], *Ehlert et al.* [2012], *Fripiat et al.* [2011a, 2011b, 2012], *Grasse et al.* [2013], and *Reynolds et al.* [2006].

eters as well. We found that within the annually averaged surface mixed layer, $\delta^{30}Si_{DSi}$ and $\delta^{30}Si_{BSi}$ are tightly coupled by biological production. As shown in Figures 1d–1f the difference between $\delta^{30}Si_{BSi}$ and $\delta^{30}Si_{DSi}$ is nearly uniform and is equal to −1.1‰, which is the constant fractionation during opal production in the model. Beneath the mixed layer depth (if the mixed layer depth is shallower than the euphotic zone), the difference between $\delta^{30}Si_{BSi}$ and $\delta^{30}Si_{DSi}$ is decoupled from −1.1‰ in the diatom productive regions (Figures 1g–1i), due to the mixing of silicic acid with lighter $\delta^{30}Si_{DSi}$ from deeper waters. In the equatorial upwelling regions where the annual mean surface mixed layer depth is shallower than the euphotic zone, for example, the silicic acid with high $\delta^{30}Si_{DSi}$ is constrained to the mixed layer. In contrast, the biogenic opal produced within the mixed layer with high $\delta^{30}Si_{BSi}$ value partly sinks out of the mixed layer. Below the mixed layer depth (within the euphotic zone), $\delta^{30}Si_{DSi}$ is mixed with the upwelled lighter $\delta^{30}Si_{DSi}$ signal, while the $\delta^{30}Si_{BSi}$ signal is partly derived from the mixed layer. Therefore, the difference between $\delta^{30}Si_{BSi}$ and $\delta^{30}Si_{DSi}$ below the mixed layer depth can become larger than −1.1‰ (Figure 1i), which explains the signal seen in the euphotic zone (Figure 1c).

4.1.3. $\delta^{30}Si_{DSi}$ in the Deep Ocean

The $\delta^{30}Si_{DSi}$ in the deep ocean is controlled by advection related to the thermohaline circulation, mixing, and biological productivity in the surface ocean followed by export and dissolution of BSi, as shown by previous studies [*Reynolds*, 2009; *de Souza et al.*, 2012a, 2012b, 2014; *Brzezinski and Jones*, 2015; *Holzer and Brzezinski*, 2015]. Horizontal variations of $\delta^{30}Si_{DSi}$ among deep water masses have been long noted by both in situ measurements [*De La Rocha et al.*, 2000] and modeling studies [*Reynolds*, 2009; *Matsumoto et al.*, 2013]. Our model captures a clear $\delta^{30}Si_{DSi}$ gradient between the deep North Atlantic and the deep North Pacific (Figure 3). However, in the deep North Pacific the modeled average value of +1.1‰ appears higher than the observed value of +0.9‰ [*De La Rocha et al.*, 2000]. Some other modeling studies also show higher $\delta^{30}Si_{DSi}$ values in the deep Pacific compared to observations [*Matsumoto et al.*, 2013; *de Souza et al.*, 2014]. The origin of the observed low $\delta^{30}Si_{DSi}$ remains unknown. *De Souza et al.* [2014] have suggested that either there is higher nutrient supply to the surface subarctic Pacific than simulations are able to reproduce or that the deep North Pacific $\delta^{30}Si_{DSi}$ values may be influenced by DSi derived from hydrothermal sources.

There is a clear meridional gradient of $\delta^{30}Si_{DSi}$ in the deep Atlantic Ocean (Figure 3), which can be attributed to the quasi-conservative mixing of the isotopically heavy NADW and the isotopically light Antarctic Bottom Water (AABW) [*de Souza et al.*, 2012b, 2014; *Brzezinski and Jones*, 2015; *Holzer and Brzezinski*, 2015]. The approximately linear relationship between the inverse silicic acid concentration and $\delta^{30}Si_{DSi}$ below 1000 m depth in the Atlantic simulated by our model agrees well with observations (Figure 9). The inclusion of fractionation

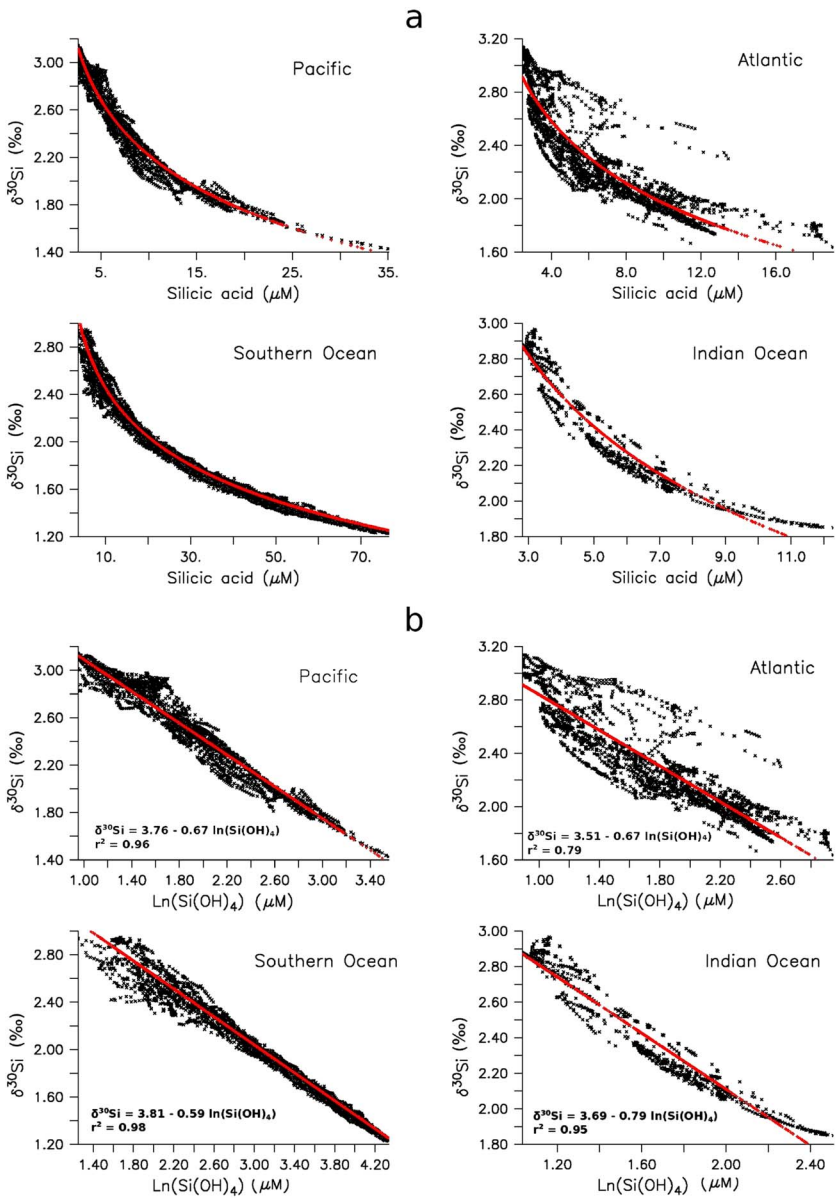

Figure 8. (a) δ^{30}Si (‰) in upper 90 m water column versus silicic acid concentration (μmol L^{-1}) in four different ocean basins and (b) δ^{30}Si (‰) versus natural logarithm of silicic acid concentration (μmol L^{-1}) in the according ocean basins. The red lines are linear regression curves of δ^{30}Si versus ln($Si(OH)_4$) in all panels, and the *y* intercepts of the regression lines are in per mil (‰) unit.

during opal dissolution in our model does not improve the agreement with observations, which is in contrast to the findings of *Holzer and Brzezinski* [2015], based on a different model system.

4.2. Seasonal Dynamics of δ^{30}Si

As our model simulates biogenic silica production prognostically, it allows us to examine the seasonal cycle of δ^{30}Si. We find that there is a substantial seasonal variation in $\delta^{30}Si_{DSi}$, which can be up to 0.7‰. This should be taken into account when comparing observed δ^{30}Si with model output.

The seasonal cycles of $\delta^{30}Si_{DSi}$ and $\delta^{30}Si_{BSi}$ are coupled in time with silicic acid concentration and mixed layer depth (Figure 10). Taking the North Atlantic (defined here as 40°N–80°N, 70°W–20°E) as an example, the winter mixed layer reaches its largest depth around March, which brings nutrient-enriched water with lighter $\delta^{30}Si_{DSi}$ to the surface. Abundant nutrients generally lead to a diatom spring bloom that then causes a maximum biogenic opal export in May. During the intensive utilization of silicic acid in spring, the preferential

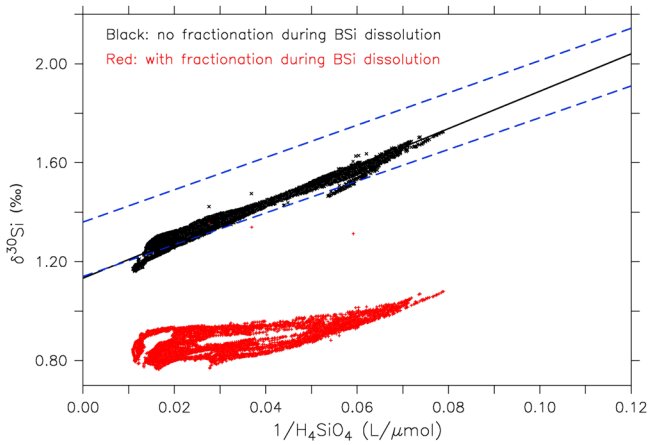

Figure 9. Modeled δ^{30}Si (‰) versus inverse silicic acid concentration (L (μmol) $^{-1}$) in the Atlantic (41°S–70°N, 0°W–61°W) below 1000 m depth (scattered crosses in black), with the linear regression (solid black line). The blue dashed lines are linear regressions of the measurements in the Atlantic from *Brzezinski and Jones* [2015] (the upper line) and *de Souza et al.* [2012b] (the lower line) (data points are not shown here). The red scattered crosses are results from a model run which includes fractionation during biogenic opal dissolution.

uptake of the lighter silicon isotopes elevates the $\delta^{30}Si_{DSi}$ in the surface water. The $\delta^{30}Si_{DSi}$ increases until September due to the continued uptake of silicic acid by diatoms and the water column stratification. The $\delta^{30}Si_{BSi}$ follows the trend of $\delta^{30}Si_{DSi}$ in time. In both hemispheres the surface, seasonally dependent $\delta^{30}Si_{DSi}$ and $\delta^{30}Si_{BSi}$ are inversely related to DSi concentration and mixed layer depth and peak approximately four months after the BSi export reaches its maximum, likely due to the continued uptake by diatoms and the water column stratification. This demonstrates that the biological fractionation and the physical transport of waters are two major controlling factors of δ^{30}Si also over seasonal time scales.

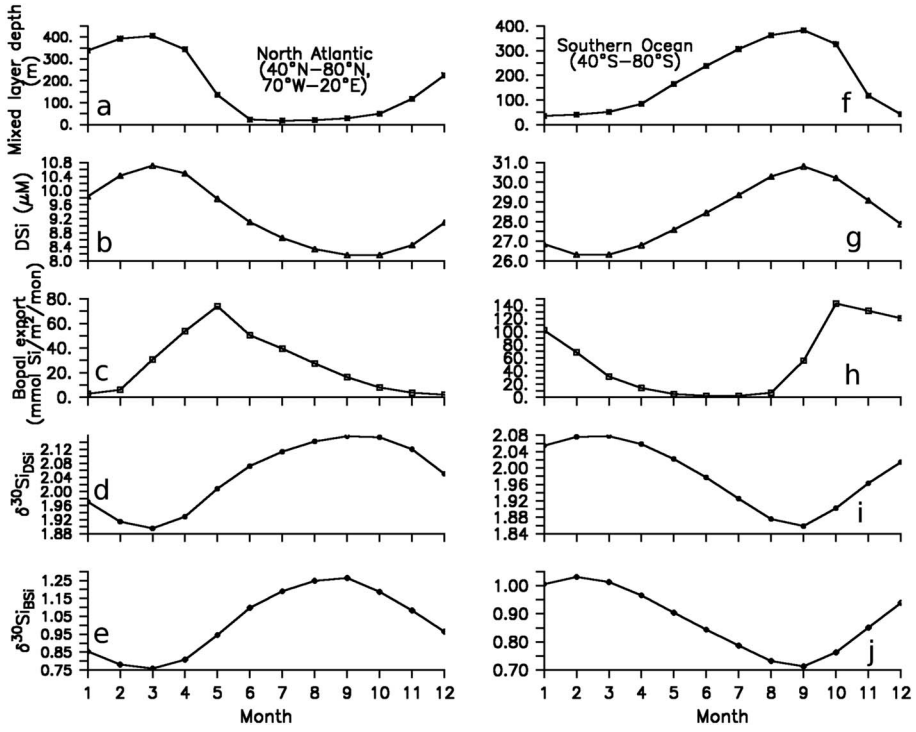

Figure 10. Seasonal variations of the (a, f) mixed layer depth (m), (b, g) silicic acid concentration (μmol L^{-1}) (averaged in the upper 90 m water depth), (c, h) biogenic opal export (mmol Si m^{-2}), (d, i) the δ^{30}Si (‰) of silicic acid (averaged in the upper 90 m water depth), and (e, j) the δ^{30}Si (‰) of biogenic opal (averaged in the upper 90 m water depth) in the North Atlantic (Figures 10a–10e) and in the Southern Ocean (Figures 10f–10j).

4.3. Control of δ^{30}Si Distribution in the Sediments

Figure 5b shows that the pattern of $\delta^{30}Si_{BSi}$ on the sediment surface reflects the $\delta^{30}Si_{BSi}$ signature produced in the euphotic zone. This model behavior validates the assumption made in paleoreconstructions that the sedimentary $\delta^{30}Si_{BSi}$ signal indicates the extent of silicic acid utilization by diatoms in the surface ocean, at least under the assumption that no further fractionation occurs during diagenesis. It is important to note that the exported $\delta^{30}Si_{BSi}$ from euphotic zone can differ by up to 0.24‰ from what is produced in the mixed layer, if the mixed layer is shallower than the euphotic zone. This is because in regions where the mixed layer is shallower than the euphotic zone, the δ^{30}Si of BSi which is produced below the mixed layer has a relatively lighter signal.

The fully prognostic sediment model provides us also the possibility to study the interaction between the ocean and the sediment concerning the δ^{30}Si signal. The δ^{30}Si of silicic acid in the ocean bottom layer outside of the Arctic Ocean is mostly homogeneous with an average value of +1.20‰ (Figure 4a), which very likely originates from the Southern Ocean and is transported northward by the AABW. As we have mentioned before, our model has a strong invasion of AABW into the deep North Atlantic compared to observations. In reality, $\delta^{30}Si_{DSi}$ in the ocean bottom layer of the North Atlantic might be higher due to the influence of NADW. The Arctic bottom water has the highest $\delta^{30}Si_{DSi}$ value among all ocean basins, which is in accordance with the findings of *Brzezinski and Jones* [2015] and *Holzer and Brzezinski* [2015]. The pore water diffusion acts as a low $\delta^{30}Si_{DSi}$ source to the bottom water of the Arctic Ocean.

The $\delta^{30}Si_{DSi}$ value of pore water in the sediment surface layer has a spatial pattern similar to $\delta^{30}Si_{BSi}$ in the sediment (Figure 4b), which reflects the exported $\delta^{30}Si_{BSi}$ signal from the euphotic zone. In the Southern Ocean south of the polar front, the surface water has high silicic acid concentration with a low $\delta^{30}Si_{DSi}$ signature due to the wind-driven upwelling ventilating deep waters with light $\delta^{30}Si_{DSi}$. Thus, the δ^{30}Si value of opal that is produced from this surface water is even lower. The nutrient-enriched surface water flows equatorward from the Antarctic Divergence driven by the Ekman drift. Meanwhile, silicic acid is strongly depleted by diatoms, which results in a relatively high signal of the exported $\delta^{30}Si_{BSi}$ sinking into the sediment. Additionally, in the Southern Hemisphere subtropical gyres silicic acid is further depleted, which produces the highest $\delta^{30}Si_{BSi}$ value in the sediment. Therefore, as shown in Figure 4c that the sediment pore water is a source of low $\delta^{30}Si_{DSi}$ to the ocean bottom water in the Southern Ocean, while it acts as a source of high $\delta^{30}Si_{DSi}$ to the bottom water in the Southern Hemisphere subtropical gyres.

5. Summary and Conclusions

Our work offers some new insights of the modern oceanic δ^{30}Si distribution and its controlling mechanisms, in terms of seasonality and sediment dynamics. The model results agree with previous studies that the biological fractionation during biogenic silica production and physical transport and mixing of water masses are two essential factors for controlling $\delta^{30}Si_{DSi}$ distributions over time scales ranging from seasonal to that of the overturning circulation. There is a distinct seasonal cycle of $\delta^{30}Si_{DSi}$ and $\delta^{30}Si_{BSi}$ in surface waters, and they inversely covary with silicic acid concentration and the mixed layer depth in time. The seasonal variation in $\delta^{30}Si_{DSi}$ should be taken into account when comparing in situ data with model results. The sedimentary $\delta^{30}Si_{BSi}$ distribution reflects the exported signal from the euphotic zone in the model. This opens a possibility to reconstruct the oceanic δ^{30}Si in past climate conditions with the help of sedimentary proxy data, under the assumptions that opal frustules sink down through the water column without significant horizontal redistribution and no further fractionation during sediment diagenesis. Sediment pore water diffusion induced by dissolution of biogenic silica in the sediment acts as a source of light δ^{30}Si into the bottom waters of the Arctic and Southern Ocean, while it is a source of heavy δ^{30}Si to the Southern Hemisphere subtropical gyres. A relatively coarse resolution is used for this modern simulation because of the expensive computation and long equilibrium time. A simulation with a finer resolution may improve the nutrient distribution by avoiding high diffusivity, e.g., in the Southern Ocean.

Acknowledgments

This work was supported by the China Scholarship Council. The authors thank Ernst Maier-Reimer for the fruitful discussion at an early stage of this work. Our thanks to Nicolas Gruber (nicolas.gruber@env.ethz.ch) for providing the data of estimates of particulate organic carbon and biogenic opal export fluxes. Other data used for model-observation comparison were extracted from the publications of *Beucher et al.* [2008, 2011], *Cardinal et al.* [2005], *De La Rocha et al.* [2000, 2011], *de Souza et al.* [2012a, 2012b], *Ehlert et al.* [2012], *Fripiat et al.* [2011a, 2011b, 2012], *Grasse et al.* [2013], and *Reynolds et al.* [2006]. We thank Gregory de Souza, Katsumi Matsumoto, and two anonymous reviewers for their constructive reviews.

References

Bernard, C. Y., H. H. Dürr, C. Heinze, J. Segschneider, and E. Maier-Reimer (2011), Contribution of riverine nutrients to the silicon biogeochemistry of the global ocean—A model study, *Biogeosciences*, *8*(3), 551–564, doi:10.5194/bg-8-551-2011.

Beucher, C. P., M. A. Brzezinski, and X. Crosta (2007), Silicic acid dynamics in the glacial sub-Antarctic: Implications for the silicic acid leakage hypothesis, *Global Biogeochem. Cycles*, *21*, GB3015, doi:10.1029/2006GB002746.

Beucher, C. P., M. A. Brzezinski, and J. L. Jones (2008), Sources and biological fractionation of Silicon isotopes in the Eastern Equatorial Pacific, *Geochim. Cosmochim. Acta*, *72*(13), 3063–3073.

Beucher, C. P., M. A. Brzezinski, and J. L. Jones (2011), Mechanisms controlling silicon isotope distribution in the Eastern Equatorial Pacific, *Geochim. Cosmochim. Acta*, *75*(15), 4286–4294.
Brzezinski, M. A., and J. L. Jones (2015), Coupling of the distribution of silicon isotopes to the meridional overturning circulation of the North Atlantic Ocean, *Deep Sea Res., Part II*, *116*, 79–88.
Brzezinski, M. A., C. J. Pride, V. M. Franck, D. M. Sigman, J. L. Sarmiento, K. Matsumoto, N. Gruber, G. H. Rau, and K. H. Coale (2002), A switch from $Si(OH)_4$ to NO_3^- depletion in the glacial Southern Ocean, *Geophys. Res. Lett.*, *29*(12), 1564, doi:10.1029/2001GL014349.
Buesseler, K. O. (1998), The decoupling of production and particulate export in the surface ocean, *Global Biogeochem. Cycles*, *12*(2), 297–310.
Cardinal, D., L. Y. Alleman, F. Dehairs, N. Savoye, T. W. Trull, and L. André (2005), Relevance of silicon isotopes to Si-nutrient utilization and Si-source assessment in Antarctic waters, *Global Biogeochem. Cycles*, *19*, GB2007, doi:10.1029/2004GB002364.
Cardinal, D., N. Savoye, T. W. Trull, F. Dehairs, E. E. Kopczynska, F. Fripiat, J.-L. Tison, and L. André (2007), Silicon isotopes in spring Southern Ocean diatoms: Large zonal changes despite homogeneity among size fractions, *Mar. Chem.*, *106*(1–2), 46–62.
Cavagna, A. J., F. Fripiat, F. Dehairs, D. Wolf-Gladrow, B. Cisewski, N. Savoye, L. André, and D. Cardinal (2011), Silicon uptake and supply during a Southern Ocean iron fertilization experiment (EIFEX) tracked by Si isotopes, *Limnol. Oceanogr.*, *56*(1), 147–160.
Coplen, T. B., et al. (2002), Compilation of minimum and maximum isotope ratios of selected elements in naturally occurring terrestrial materials and reagents, *Water Resour. Invest. Rep. 01-4222*, U.S Department of the Interior and U.S Geological Survey, Vancouver.
De La Rocha, C. L., M. A. Brzezinski, and M. J. DeNiro (1997), Fractionation of silicon isotopes by marine diatoms during biogenic silica formation, *Geochim. Cosmochim. Acta*, *61*(23), 5051–5056.
De La Rocha, C. L., M. A. Brzezinski, M. J. DeNiro, and A. Shemesh (1998), Silicon-isotope composition of diatoms as an indicator of past oceanic change, *Nature*, *395*(6703), 680–683.
De La Rocha, C. L., M. A. Brzezinski, and M. J. DeNiro (2000), A first look at the distribution of the stable isotopes of silicon in natural waters, *Geochim. Cosmochim. Acta*, *64*(14), 2467–2477.
De La Rocha, C. L., P. Bescont, A. Croguennoc, and E. Ponzevera (2011), The silicon isotopic composition of surface waters in the Atlantic and Indian sectors of the Southern Ocean, *Geochim. Cosmochim. Acta*, *75*(18), 5283–5295.
de Souza, G. F., B. C. Reynolds, G. C. Johnson, J. L. Bullister, and B. Bourdon (2012a), Silicon stable isotope distribution traces Southern Ocean export of Si to the eastern South Pacific thermocline, *Biogeosciences*, *9*(11), 4199–4213.
de Souza, G. F., B. C. Reynolds, J. Rickli, M. Frank, M. A. Saito, L. J. A. Gerringa, and B. Bourdon (2012b), Southern Ocean control of silicon stable isotope distribution in the deep Atlantic Ocean, *Global Biogeochem. Cycles*, *26*, GB2035, doi:10.1029/2011GB004141.
de Souza, G. F., R. D. Slater, J. P. Dunne, and J. L. Sarmiento (2014), Deconvolving the controls on the deep ocean's silicon stable isotope distribution, *Earth Planet. Sci. Lett.*, *398*, 66–76.
Demarest, M. S., M. A. Brzezinski, and C. P. Beucher (2009), Fractionation of silicon isotopes during biogenic silica dissolution, *Geochim. Cosmochim. Acta*, *73*(19), 5572–5583.
Dugdale, R. C., F. P. Wilkerson, and H. J. Minas (1995), The role of a silicate pump in driving new production, *Deep Sea Res., Part I*, *42*(5), 697–719.
Dürr, H. H., M. Meybeck, J. Hartmann, G. G. Laruelle, and V. Roubeix (2011), Global spatial distribution of natural riverine silica inputs to the coastal zone, *Biogeosciences*, *8*(3), 597–620.
Ehlert, C., P. Grasse, E. Mollier-Vogel, T. Böschen, J. Franz, G. F. de Souza, B. C. Reynolds, L. Stramma, and M. Frank (2012), Factors controlling the silicon isotope distribution in waters and surface sediments of the Peruvian coastal upwelling, Geochim. Cosmochim. Acta, *99*, 128–145.
Ellwood, M. J., M. Wille, and W. Maher (2010), Glacial silicic acid concentrations in the Southern Ocean, *Science*, *330*(6007), 1088–1091.
Fripiat, F., A. J. Cavagna, F. Dehairs, S. Speich, L. André, and D. Cardinal (2011a), Silicon pool dynamics and biogenic silica export in the Southern Ocean inferred from Si-isotopes, *Ocean Sci.*, *7*(5), 533–547.
Fripiat, F., A.-J. Cavagna, N. Savoye, F. Dehairs, L. André, and D. Cardinal (2011b), Isotopic constraints on the Si-biogeochemical cycle of the Antarctic Zone in the Kerguelen area (KEOPS), *Mar. Chem.*, *123*(1–4), 11–22.
Fripiat, F., A.-J. Cavagna, F. Dehairs, A. de Brauwere, L. André, and D. Cardinal (2012), Processes controlling the Si-isotopic composition in the Southern Ocean and application for paleoceanography, *Biogeosciences*, *9*(7), 2443–2457.
Gao, S. (2014), Mechanistic understanding of the marine biogeochemical proxy δ^{30}Si: A modeling approach, PhD thesis, Univ. of Bremen, Bremen, Germany.
Garcia, H. E., R. A. Locarnini, T. P. Boyer, J. I. Antonov, M. M. Zweng, O. K. Baranova, and D. R. Johnson (2010), World Ocean Atlas 2009, Volume 4: Nutrients (phosphate, nitrate, silicate), in *Tech. Rep., NOAA Atlas NESDIS 71*, edited by S. Levitus, 398 pp., U.S. Gov. Print. Off., Washington, D. C.
Gent, P. R., J. Willebrand, T. J. McDougall, and J. C. McWilliams (1995), Parameterizing eddy-induced tracer transports in ocean circulation models, *J. Phys. Oceanogr.*, *25*(4), 463–474.
Gnanadesikan, A. (1999), A global model of silicon cycling: Sensitivity to eddy parameterization and dissolution, *Global Biogeochem. Cycles*, *13*(1), 199–220.
Grasse, P., C. Ehlert, and M. Frank (2013), The influence of water mass mixing on the dissolved Si isotope composition in the Eastern Equatorial Pacific, *Earth Planet. Sci. Lett.*, *380*, 60–71.
Heinze, C., E. Maier-Reimer, A. M. E. Winguth, and D. Archer (1999), A global oceanic sediment model for long-term climate studies, *Global Biogeochem. Cycles*, *13*(1), 221–250.
Holzer, M., and M. A. Brzezinski (2015), Controls on the silicon isotope distribution in the ocean: New diagnostics from a data-constrained model, *Global Biogeochem. Cycles*, *29*, 267–287, doi:10.1002/2014GB004967.
Kamatani, A. (1982), Dissolution rates of silica from diatoms decomposing at various temperatures, *Mar. Biol.*, *68*(1), 91–96.
Legutke, S., and E. Maier-Reimer (2002), The impact of a downslope water-transport parametrization in a global ocean general circulation model, *Clim. Dyn.*, *18*, 611–623.
Maier-Reimer, E., I. Kriest, J. Segschneider, and P. Wetzel (2005), The HAMburg Ocean Carbon Cycle Model HAMOCC 5.1, *Tech. Description Release 1.1*, Max Planck Inst. for Meteorol, Hamburg.
Marsland, S. J., H. Haak, J. H. Jungclaus, M. Latif, and F. Roske (2003), The Max-Planck-Institute global ocean/sea ice model with orthogonal curvilinear coordinates, *Ocean Modell.*, *5*(2), 91–127.
Matsumoto, K., K. Tokos, A. Huston, and H. Joy-Warren (2013), MESMO 2: A mechanistic marine silica cycle and coupling to a simple terrestrial scheme, *Geosci. Model Dev.*, *6*(2), 477–494.
Milligan, A. J., D. E. Varela, M. A. Brzezinski, and F. M. M. Morel (2004), Dynamics of silicon metabolism and silicon isotopic discrimination in a marine diatom as a function of pCO_2, *Limnol. Oceanogr.*, *49*(2), 322–329.

Nelson, D. M., P. Tréguer, M. A. Brzezinski, A. Leynaert, and B. Quéguiner (1995), Production and dissolution of biogenic silica in the ocean: Revised global estimates, comparison with regional data and relationship to biogenic sedimentation, *Global Biogeochem. Cycles*, *9*(3), 359–372.

Pichevin, L. E., B. C. Reynolds, R. S. Ganeshram, I. Cacho, L. Pena, K. Keefe, and R. M. Ellam (2009), Enhanced carbon pump inferred from relaxation of nutrient limitation in the glacial ocean, *Nature*, *459*(7250), 1114–1117.

Redfield, A. C., B. H. Ketchum, and F. A. Richards (1963), The influence of organisms on the composition of sea-water, in *The Sea*, vol. 2, edited by M. N. Hill, pp. 26–77, Interscience, New York.

Reynolds, B. C. (2009), Modeling the modern marine δ^{30}Si distribution, *Global Biogeochem. Cycles*, *23*, GB2015, doi:10.1029/2008GB003266.

Reynolds, B. C., M. Frank, and A. N. Halliday (2006), Silicon isotope fractionation during nutrient utilization in the North Pacific, *Earth Planet. Sci. Lett.*, *244*(1–2), 431–43.

Sarmiento, J. L., and N. Gruber (Eds.) (2006), *Ocean Biogeochemical Dynamics*, Princeton Univ. Press, Princeton, N. J.

Six, K. D., and E. Maier-Reimer (1996), Effects of plankton dynamics on seasonal carbon fluxes in an ocean general circulation model, *Global Biogeochem. Cycles*, *10*(4), 559–583.

Smetacek, V. (1999), Diatoms and the ocean carbon cycle, *Protist*, *150*(1), 25–32.

Sutton, J. N., D. E. Varela, M. A. Brzezinski, and C. P. Beucher (2013), Species-dependent silicon isotope fractionation by marine diatoms, *Geochim. Cosmochim. Acta*, *104*, 300–309.

Tréguer, P. J., and C. L. De La Rocha (2013), The world ocean silica cycle, *Annu. Rev. Mar. Sci.*, *5*(1), 477–501, doi:10.1146/annurev-marine-121211-172346.

Varela, D. E., C. J. Pride, and M. A. Brzezinski (2004), Biological fractionation of silicon isotopes in Southern Ocean surface waters, *Global Biogeochem. Cycles*, *18*, GB1047, doi:10.1029/2003GB002140.

Wischmeyer, A. G., C. L. De La Rocha, E. Maier-Reimer, and D. A. Wolf-Gladrow (2003), Control mechanisms for the oceanic distribution of silicon isotopes, *Global Biogeochem. Cycles*, *17*(3), 1083, doi:10.1029/2002GB002022.